J|A|C|S
ARTICLES
Published on Web 01/19/2002

Nd−Fe−B Permanent Magnet Electrodes. Theoretical Evaluation and Experimental Demonstration of the Paramagnetic Body Forces

Nicholas Leventis* and Xuerong Gao

Contribution from the Department of Chemistry, University of Missouri—Rolla, 226 Schrenk Hall, Rolla, Missouri 65409

Received September 19, 2001

Abstract: Cyclic voltammetry with Nd−Fe−B disk magnet electrodes (3.2 mm diameter) at slow sweep rates ($\leq$0.01 V s^{-1}) in relatively concentrated solutions (e.g., 80 mM) of diamagnetic redox-active species (e.g., TMPD) is controlled by diffusion. Under similar conditions, cyclic voltammetry with conventional noble metal disk millielectrodes is characterized by the absence of diffusion waves and the presence of density gradient driven natural convection. Although the magnetic field in the vicinity of Nd−Fe−B electrodes is relatively strong ($\sim$0.5 T at the surface of the magnet electrode), the absence of magnetohydrodynamic stirring effects is attributed to the fact that the **i** and **B** vectors are almost parallel, and therefore the magnetohydrodynamic force $\mathbf{F}_B$ ($=\mathbf{i} \times \mathbf{B}$) is very small. On the other hand, the absence of natural convection is attributed to the two possible paramagnetic body forces, $\mathbf{F}_{\nabla B}$ and $\mathbf{F}_{\nabla C}$, exerted by the magnet electrode on the diffusion layer. Of those two forces, the former depends on field gradients ($\mathbf{F}_{\nabla B} \sim \mathbf{B}\cdot\nabla\mathbf{B}$), while the latter depends on concentration gradients ($\mathbf{F}_{\nabla C} \sim \nabla C_j$) and is directed toward areas with higher concentration of paramagnetic *j*. Through thorough analysis of the magnetic field and its gradients, it is found that the average $\mathbf{F}_{\nabla C}$ force acting upon the entire diffusion layer is $\sim$1.75 times stronger than $\mathbf{F}_{\nabla B}$. Nevertheless, it is calculated that either force independently is strong enough and would have been able to hold the diffusion layer by itself. Further evidence suggests that, integrated over the entire solution, $\mathbf{F}_{\nabla B}$ is the dominant paramagnetic force when the redox-active species is paramagnetic, e.g., $[Co(bipy)_3](ClO_4)_2$ (bipy = 2,2′-bipyridine). Finally, convective behavior with diamagnetic redox-active species and magnet millielectrodes can be observed by holding closely (2−3 mm away) a repelling second magnet that bends the induction **B** to the point that the $\mathbf{i} \times \mathbf{B}$ product is not equal to 0.

1. Introduction

Nd−Fe−B permanent magnets are compact and inexpensive, with the highest magnetization and the most competitive cost per unit-energy product of all magnets.[1] As we reported recently,[2] electrolysis with noble metal millielectrodes in the field of such magnets generally yields strong stirring effects in the electrolytic solution, similar to those observed with large (and expensive) electromagnets.[3−8] The main cause of this stirring is the magnetohydrodynamic (MHD) force, $\mathbf{F}_B$, which is given by eq 1, where **i** is the current density flowing through the electrolytic conductor and **B** the magnetic flux density.[9]

$$\mathbf{F}_B = \mathbf{i} \times \mathbf{B} \tag{1}$$

Since Nd−Fe−B is a metallic alloy, the question that arises naturally is whether small Nd−Fe−B disk magnets could be used as electrodes directly, and, if so, what would the effects be, if any. As it turns out, the most startling phenomenon during electrolysis of diamagnetic species with Nd−Fe−B electrodes is that the current−voltage characteristics are *diffusion-controlled* at conditions where noble metal electrodes of similar size produce voltammograms dominated by natural convection.

Natural convection in electrolytic solutions arises from the density difference between the diffusion layer and the surrounding liquid. Due to this density difference, the diffusion layer

* Address correspondence to this author. Tel.: 573-341-4391. Fax.: 573-341-6033. E-mail: leventis@umr.edu.

(1) Craik, D. *Magnetism, Principles and Applications*; Wiley: New York, 1995; (a) p 386, (b) p 29, (c) p 312.
(2) Leventis, N.; Gao, X. *Anal. Chem.* **2001**, *73*, 3981.
(3) (a) Mohanta, S.; Fahidy, T. Z. *Can. J. Chem. Eng.* **1972**, *50*, 248. (b) Fahidy, T. Z. *J. Appl. Electrochem.* **1983**, *13*, 553.
(4) Aogaki, R.; Fueki, K.; Mukaibo, T. *Denki Kagaku* **1976**, *44*, 89.
(5) (a) Aaboubi, O.; Chopart, J. P.; Douglade, J.; Olivier, A.; Gabrielli, C.; Tribollet, B. *J. Electrochem. Soc.* **1990**, *137*, 1796. (b) Chopart, J. P.; Douglade, J.; Fricoteaux, P.; Olivier, A. *Electrochim. Acta* **1991**, *36*, 459. (c) Fricoteaux, P.; Olivier, A.; Delmas, R. *J. Electrochem. Soc.* **1992**, *139*, 1096.
(6) Tacken, R. A.; Janssen, L. J. J. *J. Appl. Electrochem.* **1995**, *25*, 1.
(7) (a) Lee, J.; Gao, X.; Hardy, L. D. A.; White, H. S. *J. Electrochem. Soc.* **1995**, *142*, L90. (b) Ragsdale, S. R.; Lee, J.; Gao, X.; White, H. S. *J. Phys. Chem.* **1996**, *100*, 5913. (c) Lee, J.; Ragsdale, S. R.; Gao, X.; White, H. S. *J. Electroanal. Chem.* **1997**, *422*, 169. (d) Ragsdale, S. R.; Lee, J.; White, H. S. *Anal. Chem.* **1997**, *69*, 2070. (e) Ragsdale, S. R.; White, H. S. *Anal. Chem.* **1999**, *71*, 1923. (f) Grant, K. M.; Hemmert, J. W.; White, H. S. *J. Electroanal. Chem.* **2001**, *500*, 95.
(8) (a) Leventis, N.; Chen, M.; Gao, X.; Canalas, M.; Zhang, P. *J. Phys. Chem. B* **1998**, *102*, 3512. (b) Leventis, N.; Gao, X. *J. Phys. Chem. B* **1999**, *103*, 5832.
(9) (a) Newman, J. S. *Electrochemical Systems*, 2nd ed.; Prentice Hall: Englewood Cliffs, NJ, 1991; Chapter 15. (b) Roberts, P. H. *An Introduction to Magnetohydrodynamics*; Elsevier Publishing Co., Inc.: New York, 1967; Chapter 1. (c) Binder, R. C. *Advanced Fluid Dynamics and Fluid Machinery*; Prentice-Hall: New York, 1951; Chapter 1.

tends to rise or fall, producing stirring.[10a] As discussed herewith, however, the magnetic field of Nd−Fe−B magnet electrodes may attract and retain the diffusion layer in contact with the electrode, preventing the effects of natural convection. For example, disk electrodes (3.2 mm diameter) made of Nd−Fe−B magnets demonstrate diffusion-controlled behavior in CH_3CN/0.5 M $LiClO_4$ containing 80 mM *N*,*N*′,*N*″,*N*‴-tetramethyl-*p*-phenylenediammine (TMPD), even with potential sweep rates as low as 0.005 V s^{-1}; under the same conditions, electrochemistry with conventional noble metal millielectrodes is dominated by natural convection. Eventually, it is shown that convective behavior and quasi steady-state voltammograms with 80 mM TMPD and magnet millielectrodes can be observed by using a second magnet held opposite to the magnet electrode and with the same poles of the two magnets facing each other. All of these phenomena have been attributed to the paramagnetic body force, $\mathbf{F}_\nabla$, that is exerted upon every unit volume element that contains paramagnetic species (e.g., radicals).[11] $\mathbf{F}_\nabla$ is the sum of two forces, $\mathbf{F}_{\nabla B}$ and $\mathbf{F}_{\nabla C}$, which, if the paramagnetic species is a free radical *j* with spin equal to $^1/_2$, are given by eqs 2 and 3 respectively.[12]

$$\mathbf{F}_{\nabla B} = 2N_A C_j[(g\mu_B)^2/4kT]\mathbf{B}\cdot\nabla\mathbf{B} \quad (2)$$

$$\mathbf{F}_{\nabla C} = N_A[(g\mu_B)^2/4kT]|\mathbf{B}|^2\nabla C_j \quad (3)$$

N_A is Avogadro's number, *g* the spectroscopic splitting factor, μ_B the Bohr magneton, *k* the Boltzmann constant, *T* the absolute temperature, and C_j the concentration of *j*.[2,14,15] $\mathbf{F}_{\nabla B}$ is present when $\mathbf{B}\cdot\nabla\mathbf{B} \neq 0$, and tends to move magnetized volumes of electrolyte toward areas where the magnetic field is more intense. The hydrodynamic effects of $\mathbf{F}_{\nabla B}$ have been considered by several investigators.[2,16,17] Importantly, White and co-workers have also attributed certain phenomena associated with focusing of radicals around ferromagnetic disk and wire microelectrodes (of diameter ≤ 250 μm) to $\mathbf{F}_{\nabla B}$-type of forces exerted by the magnetic field gradient ($\mathbf{B}\cdot\nabla\mathbf{B}$) on individual magnetic dipoles (radicals).[13,18] Although these forces comprise the origin of the $\mathbf{F}_{\nabla B}$ body force, nevertheless they do not account fully for the "lifting" power of the magnet electrodes of this study: natural convection, a phenomenon due solely to body forces, is prevented by the sum of all counter body forces acting upon the solution, namely $\mathbf{F}_{\nabla B}$ and $\mathbf{F}_{\nabla C}$. Summing all the $\mathbf{F}_{\nabla B}$-type forces acting on individual dipoles yields the $\mathbf{F}_{\nabla B}$ body force (eq 2), but not $\mathbf{F}_{\nabla C}$.[2,13] Furthermore, as it is demonstrated experimentally and discussed theoretically on the basis of the magnitude of the $\mathbf{B}\cdot\nabla\mathbf{B}$ vector for permanent magnet electrodes of the dimensions employed here, the mode of magnetophoretic mass transfer introduced by the $\mathbf{F}_{\nabla B}$-type forces on individual radicals does not compete with diffusion, which is shown to be the only mode of mass transfer in the paramagnetically confined depletion layer. Now, $\mathbf{F}_{\nabla C}$ is a force that has been described mostly mathematically.[2,14,19] According to eq 3, $\mathbf{F}_{\nabla C}$ should be present even in homogeneous fields, and it should be applied on volume elements containing a concentration gradient of paramagnetic species. $\mathbf{F}_{\nabla C}$ tends to move such volume elements in the direction of increasing radical concentration. In contrast to $\mathbf{F}_{\nabla B}$, $\mathbf{F}_{\nabla C}$ does not have a microscopic analogue and arises solely by the gradient of magnetization in the volume element,[14] which behaves as a hypothetical magnet with different pole sizes. An analogous situation in the electric field has been described for media of inhomogeneous dielectric constant.[20] Based on a quantitative comparison of $\mathbf{F}_{\nabla B}$ and $\mathbf{F}_{\nabla C}$, in this paper it is concluded that $\mathbf{F}_{\nabla C}$ acting upon the diffusion layer of magnet millielectrodes is a stronger force than $\mathbf{F}_{\nabla B}$. Integrated over the entire solution, $\mathbf{F}_{\nabla B}$ may become a stronger force than $\mathbf{F}_{\nabla C}$ if the solution contains paramagnetic species. To our knowledge, this report comprises the first quantitative evaluation of the relative significance of $\mathbf{F}_{\nabla B}$ and $\mathbf{F}_{\nabla C}$.

2. Experimental Section

Acetonitrile, $LiClO_4$, $NaClO_4$, and TMPD were purchased from Aldrich. $LiClO_4$ and $NaClO_4$ were dried overnight under vacuum at 60 °C. TMPD was sublimed before use. $[Co(bipy)_3](ClO_4)_2$ was synthesized by a modification of a literature procedure:[21] $CoCl_2\cdot 6H_2O$ (Aldrich, 1.2 g) was dissolved under N_2 in 100 mL of previously boiled and N_2-bubbling degassed warm ethanol. The solution was filtered at room temperature under N_2. The clear filtrate was added to a solution of 2,2′-dipyridyl (2.4 g) in hot ethanol (40 mL), and the resulting solution was diluted with 150 mL of deaerated distilled water. Subsequently, five molar excess of solid $NaClO_4$ (7.084 g) was added with stirring until fully dissolved. The solution was cooled in an ice bath for 50 min and filtered. The product was dried under vacuum at 50 °C. Received 3.2 g (87% yield). Elemental analysis. Found: C, 49.60; H, 3.12; N, 11.53. Calculated for $C_{30}H_{24}O_8N_6Cl_2Co$: C, 49.62; H, 3.30; N, 11.57.

Electrochemical experimentation was carried out in Ar-degassed solutions in a homemade faradaic cage using a Perkin-Elmer 263A potentiostat and the Perkin-Elmer Model 270/250 Research Electrochemical Software 4.30. The solution resistance was measured with the electrochemical software package, and an 85% compensation was applied automatically by the potentiostat. A Au disk electrode (2 mm diameter) and an aqueous Ag/AgCl reference electrode were purchased from CH Instruments, Inc. (Austin, TX). The counter electrode was a gold foil (4 cm^2 on both sides). Nd−Fe−B magnet electrodes were made as follows.

Tiny cylindrical Nd−Fe−B magnets of two different dimensions (3.2 mm diameter, 1.6 mm height and 4.8 mm diameter, 1.6 mm height)

(10) Bard, A. J.; Faulkner, L. R. *Electrochemical Methods, Fundamentals and Applications*, 2nd ed.; John Wiley and Sons: New York, 2000; (a) p 316, (b) p 480, (c) p 231.
(11) There is also an analogous diamagnetic force, which is ~1000-fold weaker than $\mathbf{F}_\nabla$ and is not considered further.
(12) $\mathbf{F}_{\nabla B}$ has been referred to as magnetic gradient force,[13] or as field gradient force,[14] while $\mathbf{F}_{\nabla C}$ has been referred to as paramagnetic gradient force.[14] In our opinion, since manifestation of both forces requires the presence of paramagnetic species, they are both paramagnetic forces. More appropriate names would have been *field gradient body force* for the former—to distinguish from similar forces on individual molecular or ionic magnetic dipoles[13]—and *concentration gradient force* for the latter.
(13) Pullins, M. D.; Grant, K. M.; White, H. S. *J. Phys. Chem. B* **2001**, *105*, 8989.
(14) Hinds, G.; Coey, J. M. D.; Lyons, M. E. G. *Electrochem. Commun.* **2001**, *3*, 215.
(15) Equations 2 and 3 have been derived assuming that $(g\mu_B)^2|\mathbf{B}|/4kT \ll 1$,[2] which is typically true for magnetization conditions far from saturation like those encountered in electrochemistry ($|\mathbf{B}| \approx 1-2$ T and $T \approx 298$ K). It is noted further that since the molar magnetic susceptibility, χ, is given by $\chi = \mu_o N_A(g\mu_B)^2/2kT$,[1b] $\mathbf{F}_{\nabla B}$ and $\mathbf{F}_{\nabla C}$ can be expressed equivalently by $\mathbf{F}_{\nabla B} = C_j(\chi/\mu_o)\mathbf{B}\cdot\nabla\mathbf{B}$ and $\mathbf{F}_{\nabla C} = (\chi/2\mu_o)|\mathbf{B}|^2\nabla C_j$, where μ_o ($=4\pi \times 10^{-7}$ N A^{-2}) is the permeability of free space.[14]
(16) (a) O'Brien, R. N.; Santhanam, K. S. V. *J. Appl. Electrochem.* **1990**, *20*, 427. (b) O'Brien, R. N.; Santhanam, K. S. V. *J. Appl. Electrochem.* **1997**, *27*, 573.
(17) Ragsdale, S. R.; Grant, K. M.; White, H. S. *J. Am. Chem. Soc.* **1998**, *120*, 13461.
(18) Grant, K. M.; Hennert, J. W.; White, H. S. *Electrochem. Commun.* **1999**, *1*, 319.
(19) Waskaas, M.; Kharkats, Y. I. *J. Phys. Chem. B* **1999**, *103*, 4876.
(20) Breuer, M. M.; Robinson, D. *Nature* **1969**, *221*, 1116.
(21) Burstall, F. H.; Hyholm, R. S. *J. Chem. Soc.* **1952**, 3570.

Scheme 1. Nd−Fe−B Magnet Electrode with an Opposite Magnet in the Attracting (North-Facing-South) or the Repelling (South-Facing-South) Configuration

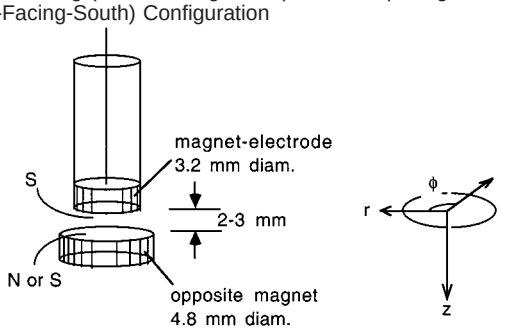

were purchased from Edmund Industrial Optics (Barrington, NJ). Such magnets were first cleaned by brief (1−2 min) successive sonications in methanol and hexane, and then they were sputter-coated with ca. 1 μm of gold using a Baltek MED 20 Sputtering System. For this, the magnets were placed approximately 4 cm directly underneath the water-cooled gold target that was sputtered with an argon plasma (60 mA at 5×10^{-3} Torr) for 600 s. Contact between the Au-free side of the magnet and a copper wire was made with silver paint. Subsequently, the copper wire−magnet assembly was sealed with white epoxy glue (Hysol 1C, Dexter Corp., Seabrook, NH) in a glass tube, leaving exposed only the Au-coated face of the disk magnet. The magnet electrode assembly was at no point exposed to heat. All curing of the epoxy was carried out at room temperature.

Nd−Fe−B magnet electrodes (3.2 mm diameter) were used in three configurations. In all three the magnet electrode was held vertically with the exposed Au-coated surface facing downward. In two of the three configurations, a second magnet (4.8 mm diameter) was used in close proximity to the magnet disk electrode (~2−3 mm away), and with the opposite (attracting configuration) or the same magnetic pole (repelling configuration) exposed toward the magnet electrode (Scheme 1). In both the attracting and the repelling configurations, the relative position of the two magnets was secured firmly: the magnet electrode was clamped from its long glass tube, while two different Au-sputtered disk magnets were glued on the bottom of two flat-bottomed beakers, the first one exposing its north pole, and the second one its south pole.

Close-up photography of the working electrode was carried out using Kodak 400-ASA film and a Nikkormat FT3 camera equipped with a fully extended Nikon Bellows Focusing Attachment model PB6 and an AF Nikkor 28−70 mm zoom lens set at 70 mm (*f*-stop 5.6; shutter speed 1/60 s). Dual-source illumination of the working electrode was conducted (a) from the front side directly with an Achiever model 321AZ electronic flash and (b) from the backside indirectly through diffuse reflection from a white paper illuminated with a Fiber-Lite High-Intensity Illuminator Series 180 (Dolan-Jenner Instruments, Inc.).

Numerical simulation of the magnetic field in all three configurations described above was conducted iteratively using a finite difference method and equations derived from basic electrodynamics.[2,22] Programming was carried out in FORTRAN 77. (Copies of the source code can be obtained from the corresponding author.) Tables with the computer-generated data for $|\mathbf{B}|$, B_r, B_z, $(B\cdot\nabla B)_r$, and $(B\cdot\nabla B)_z$ for the three experimental configurations of Scheme 1 are provided as Supporting Information. Vector and contour plotting was carried out with the Tecplot 8.0-0-6 software package (Amtec Engineering, Inc.).

3. The Magnetic Field of Magnet Electrodes

The magnet electrodes of this study are actually smaller than the probes of most readily available tesla meters. With such probes in contact with the magnet electrode the reading is ~0.5 T, but it is evident that this value can be used only as an order-of-magnitude estimate of the field intensity. For the quantitative analysis of the body forces that follows, the magnetic field generated by small magnet electrodes was calculated numerically. The magnetostatic potential, Φ, of any permanent magnet obeys the Laplace equation ($\nabla^2\Phi = 0$) everywhere in space, and it can be simulated iteratively using the appropriate boundary conditions as described before.[2] The external parameters needed for the simulation are the magnetization $\mathbf{M}$ and the volume of the magnet. The direction of $\mathbf{M}$ is parallel to the *z*-axis of the tiny cylindrical magnet (Scheme 1), and for the Nd−Fe−B material we used $|\mathbf{M}| = 9.7 \times 10^5$ A m^{-1}.[1a] The magnetic field intensity, $\mathbf{H}$, was obtained via $\mathbf{H} = -\nabla\Phi$. In turn, $\mathbf{B} = \mu_o(\mathbf{H} + \mathbf{M})$. Clearly, outside the magnet $\mathbf{M} = 0$, and $\mathbf{B}$ is parallel to $\mathbf{H}$.

Figure 1 shows the contour maps of $|\mathbf{B}|$ around the disk magnet electrode in the three configurations described in the Experimental Section. Arrows show the direction (not the magnitude) of $\mathbf{B}$ at their origin. The numerical values of $|\mathbf{B}|$ along the cylindrical axis of symmetry of the magnet, $B_z|_{r=0}$, agree within 3% with values calculated analytically (Figure 2).[23]

From the perspective of the body forces $\mathbf{F}_{\nabla C}$ and $\mathbf{F}_{\nabla B}$ (eqs 2 and 3, respectively), one needs to know $|\mathbf{B}|^2$ and $\mathbf{B}\cdot\nabla\mathbf{B}$ near the electrode. The former is a scalar quantity and can be estimated from the values of $|\mathbf{B}|$ on the contour lines of Figure 1, or it can be taken directly from the tabulated values in the Supporting Information. On the other hand, $\mathbf{B}\cdot\nabla\mathbf{B}$ is a vector quantity and has been mapped near the magnet electrode in Figure 3. It is noted immediately that either with a magnet electrode alone or with a magnet electrode facing a second magnet in the repelling configuration, the $\mathbf{B}\cdot\nabla\mathbf{B}$ vector is generally directed upward (toward the magnet electrode), and at the same time it first diverges outward (close to the electrode), and then converges inward (farther away from the electrode). The last property is more pronounced in the repelling configuration (Figure 3B). A more quantitative understanding of the behavior of the $\mathbf{B}\cdot\nabla\mathbf{B}$ vector comes from considering its three components in cylindrical coordinates:

$$r\text{-component:}\quad (B\cdot\nabla B)_r = B_r\,\partial B_r/\partial r + (B_\phi/r)\,\partial B_r/\partial\phi - (B_\phi)^2/r + B_z\,\partial B_r/\partial z \quad (4)$$

$$\phi\text{-component:}\quad (B\cdot\nabla B)_\phi = B_r\,\partial B_\phi/\partial r + (B_\phi/r)\,\partial B_\phi/\partial\phi - (B_rB_\phi)/r + B_z\,\partial B_\phi/\partial z \quad (5)$$

$$z\text{-component:}\quad (B\cdot\nabla B)_z = B_r\,\partial B_z/\partial r + (B_\phi/r)\,\partial B_z/\partial\phi + B_z\,\partial B_z/\partial z \quad (6)$$

Because of symmetry, $B_\phi = \partial(B_r,B_\phi,B_z)/\partial\phi = 0$ everywhere, hence $(\mathbf{B}\cdot\nabla\mathbf{B})_\phi = 0$, and both the *z*- and the *r*-components of $\mathbf{B}\cdot\nabla\mathbf{B}$ have only two terms. For example, the terms of the *z*-component are $B_r\,\partial B_z/\partial r$ and $B_z\,\partial B_z/\partial z$. Figure 4 shows the variation of $(B\cdot\nabla B)_z$ and its two contributing terms along the radius of the magnet electrode, 0.2 mm away from its surface. It is noted that (1) the sign of $(B\cdot\nabla B)_z$ is always positive, meaning that $(B\cdot\nabla B)_z$ is always directed toward the magnet;[24]

(22) DeVris, P. L. *A First Course in Computational Physics*; John Wiley and Sons: New York, NY, 1994; p 364.

(23) Outside and above the magnet, $H_z|_{r=0}$, i.e., the value of $|\mathbf{H}|$ along the *z*-axis of the magnet, is given by $H_z|_{r=0} = (|\mathbf{M}|/2)\{[[z + (l/2)]/[[z + (l/2)]^2 + r_o^2]^{1/2}] - [[z - (l/2)]/[[z - (l/2)]^2 + r_o^2]^{1/2}]\}$, where l is the thickness, r_o is the radius of the magnet, and the origin of z in this formula is at the geometric center of the magnet[1c] ($B_z|_{r=0} = \mu_o H_z|_{r=0}$).

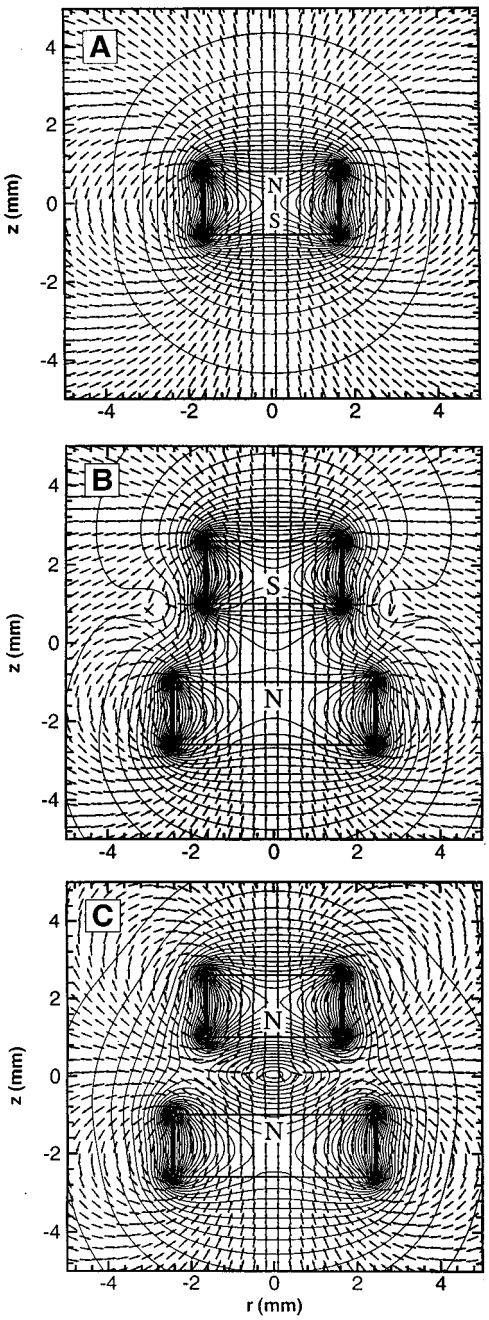

Figure 1. Digital simulation of the magnetic flux density **B** in the space around a 3.2 mm diameter, 1.6 mm thick Nd−Fe−B magnet electrode. (A) The magnet electrode alone. (B) Facing a second disk magnet (4.8 mm diameter, 1.6 mm thick) in the attracting configuration. (C) Facing the same second disk magnet in the repelling configuration. The value of $|\mathbf{B}|$ (in tesla) on the contour lines is given by $|\mathbf{B}|_n = 0.028 + (n - 1)0.028$, where n is the contour number, starting from the outmost line.

(2) the relative magnitude of the $(B\cdot\nabla B)_z$ vector in the three experimental arrangements is not very different, despite the attracting and repelling nature of the last two configurations, respectively; and (3) in all three situations $(B\cdot\nabla B)_z$ becomes very large close to the edges of the magnet. This is not difficult to reconcile: lines of force do not cross, and **B** always forms closed loops (Figure 1); therefore, near the edge of the magnet

(24) To remain consistent with the fact that the magnet electrode is always placed facing downward (Scheme 1), calculation of $(B\cdot\nabla B)_z$ and $(B\cdot\nabla B)_r$ was conducted in the fourth quadrant of the magnet electrode; thereby, the positive z-direction is toward the magnet.

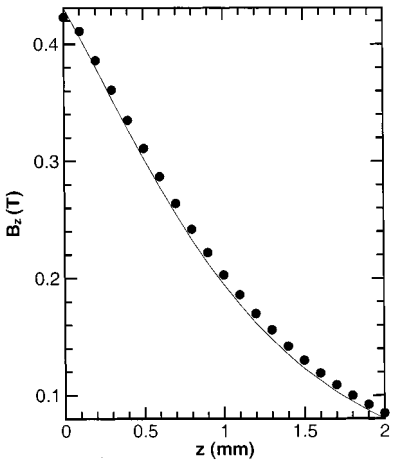

Figure 2. Comparison of analytical (continuous line) and simulated values (circles) of **B** in the z-direction above the center ($r = 0$) of the Nd−Fe−B magnet of Figure 1A. (The surface of the magnet is at $z = 0$.)

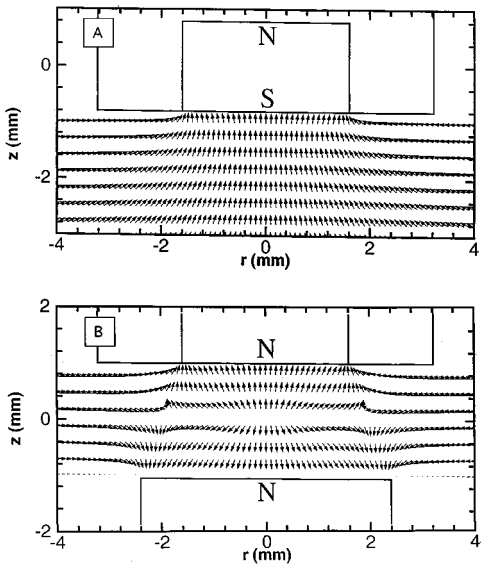

Figure 3. Maps of the $\mathbf{B}\cdot\nabla\mathbf{B}$ vector in the vicinity of the magnet electrode alone (A) or facing a second magnet in the repelling configuration (B). Arrows show the direction of the vectors; for their magnitude, refer to Figures 4 and 5. (Maps were constructed from data shown in Figure 1.)

the direction of **B** must turn toward the r-direction within short distances, thus increasing $B_r\ \partial B_z/\partial r$ to the point that it becomes the main contributor of $(B\cdot\nabla B)_z$ (refer to Figure 4, dotted line). It is noted in passing that this "edge effect" might become very large under certain circumstances. For instance, if the magnet is reduced to a 150 μm long, 50 μm diameter Nd−Fe−B wire, the value of $(B\cdot\nabla B)_z$ at the edge of the magnet ($z = 0$, $r = r_o$) is $\sim 1.33 \times 10^5$ T^2/m.

The variation of $(B\cdot\nabla B)_r$ along r (at $z = 0.2$, 0.4, and 0.6 mm from the surface of the magnet electrode) is shown in Figure 5. It is apparent that the sign (and therefore the direction) of $(B\cdot\nabla B)_r$ changes along the radius. Near the surface of a single magnet, $(B\cdot\nabla B)_r$ starts positive close to the center, i.e., pointing outward, but shortly changes its direction, pointing inward; farther from the magnet, $(B\cdot\nabla B)_r$ points only inward. Furthermore, at any level from the magnet, the expansive part of $(B\cdot\nabla B)_r$ (the part pointing outward) is weaker than its compressive part (that pointing inward). In the case of two magnets in the repelling configuration, $(B\cdot\nabla B)_r$ points outward everywhere

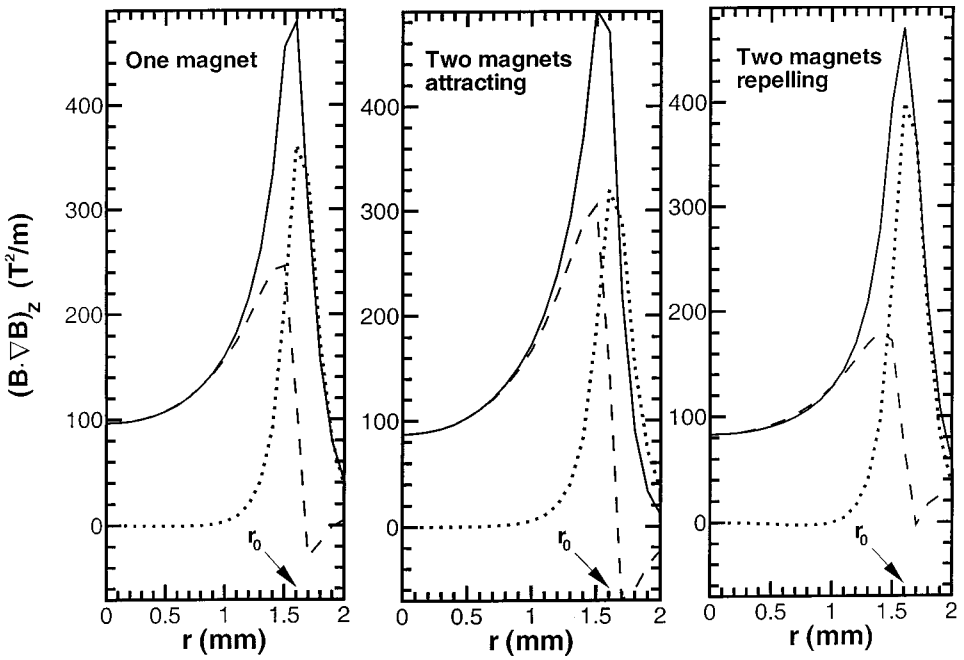

Figure 4. Variation in the *r*-direction of the $(B\cdot\nabla B)_z$ component of the $\mathbf{B}\cdot\nabla\mathbf{B}$ vector, 0.2 mm from the surface of the small magnet, in the three configurations of Figure 1. —, $(B\cdot\nabla B)_z$; – – –, $B_z\,\partial B_z/\partial z$; ···, $B_r\,\partial B_z/\partial r$. Values are shown for the fourth quadrant of the small magnet in Figure 1. Positive values indicate vectors pointing upward.

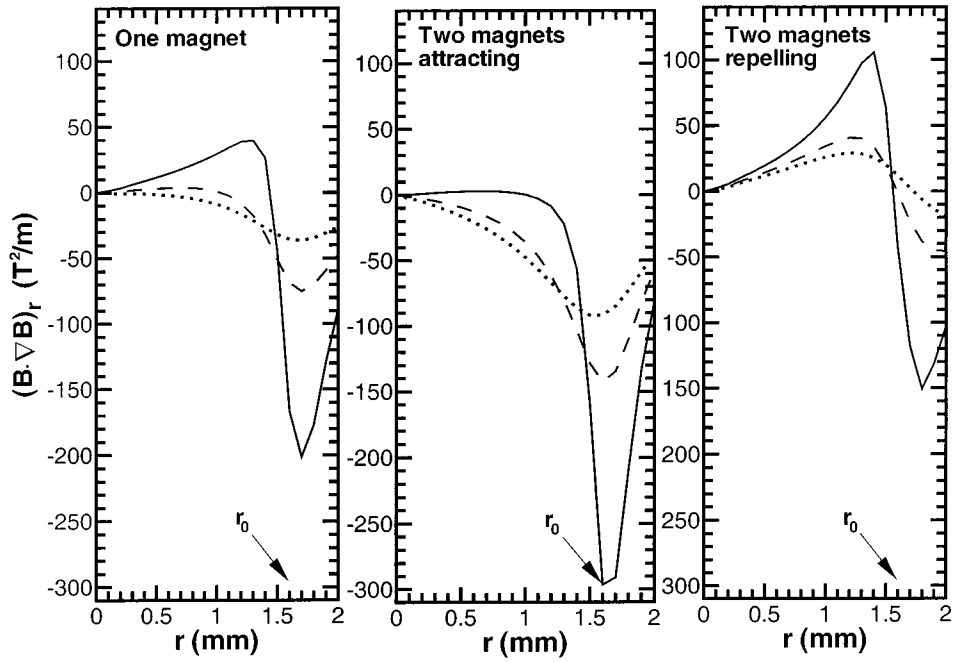

Figure 5. Variation in the *r*-direction of the $(B\cdot\nabla B)_r$ component of the $\mathbf{B}\cdot\nabla\mathbf{B}$ vector, at different distances, *z*, from the small magnet. —, $z = 0.2$ mm; – – –, $z = 0.4$ mm; ···, $z = 0.6$ mm. Values are shown for the fourth quadrant of the small magnet. Positive values indicate vectors pointing outward, negative values toward the center.

in the interval $[-r_o,r_o]$, for all *z*, and in general the expansive vectors are stronger and the compressive ones weaker than the corresponding vectors in the case of a single magnet alone or facing a second attracting magnet. (Vector maps of $(B\cdot\nabla B)_z$ and $(B\cdot\nabla B)_r$ are provided in Supporting Information as Appendix I.)

4. Results and Discussion

We have identified two apparently different kinds of electrochemical responses when magnet electrodes are used in conjunction with diamagnetic redox-active substances such as TMPD: (1) when these electrodes are used either alone or facing a second magnet in the attracting configuration and (2) when they face a second magnet in the repelling configuration.

4.1. Voltammetry with a Magnet Electrode by Itself or Facing a Second Magnet in the Attracting Configuration. One-electron oxidation of TMPD generates the cation radical $TMPD^{\bullet+}$, whose concentration is higher at the electrode and fades away in the solution defining the diffusion layer. Figure 6A shows that cyclic voltammetry in an 81 mM solution of

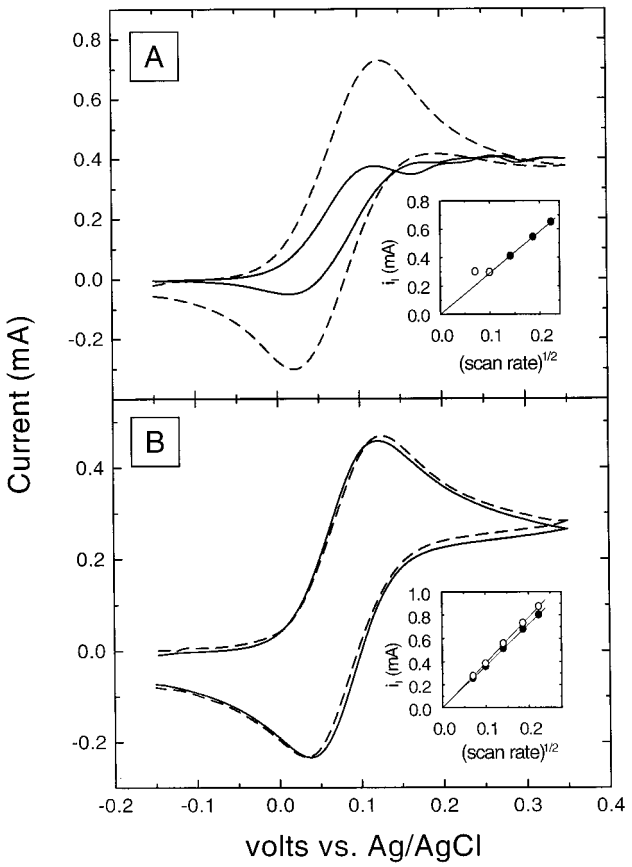

Figure 6. Cyclic voltammetry in an 81 mM solution of TMPD in CH_3CN/0.5 M $LiClO_4$. (A) Using a Au disk electrode (2 mm diameter). —, 0.01 V s^{-1}; — — —, 0.05 V s^{-1}. Inset: Randles−Sevcik plot. Dark symbols, peak currents; open symbols, plateau currents (due to no identifiable peaks). (B) Using a Nd−Fe−B disk magnet electrode (3.2 mm diameter) at 0.01 V s^{-1}. —, magnet electrode by itself; — — —, magnet electrode facing a second magnet (4.8 mm diameter) in the attracting configuration. In both cases, $i_{p,a}/i_{p,c} \approx 1.0$; $\Delta E_{p-p} \approx 75$ mV. Inset: Randles−Sevcik plots in the two experiments. (The correlation coefficient in both cases is equal to 1.0.)

TMPD in CH_3CN/0.5 M $LiClO_4$ with a Au disk millielectrode at slow sweep rates (e.g., 0.01 V s^{-1}) is characterized by the absence of diffusion waves and a quasi steady-state response that indicates the presence of (natural) convection. This is confirmed by direct observation of the electrode, using the intense blue color of electrogenerated $TMPD^{\bullet+}$ as tracer. Figure 7 (top) shows that as early as 10 s after a potential step with the Au disk electrode into the mass-transfer-controlled range (0.350 V vs Ag/AgCl), the diffusion layer has left the electrode, dropping to the bottom of the electrochemical cell. For electroneutrality reasons, the conversion of TMPD into $TMPD^{\bullet+}$ is accompanied by a diffusion layer loss of Li^+ and a gain of ClO_4^-. Since the transference number of ClO_4^- ($t_{ClO_4^-} = 0.60$) is higher than that of Li^+ ($t_{Li^+} = 0.40$),[25] more ClO_4^- ions flow into the diffusion layer than the Li^+ ions that flow out. Consequently, upon oxidation of TMPD the diffusion layer becomes "heavier"; that is, its density increases relative to the surrounding solution and falls, causing stirring. These phenomena are more pronounced as the amount of electrogenerated $TMPD^{\bullet+}$ increases, which is accomplished with a higher bulk

(25) For 1:1 electrolytes, the transference numbers are given by $t_j = \lambda_o(j)/[\lambda_o(+) + \lambda_o(-)]$, where $\lambda_o(j)$ is the limiting molar conductivity of species j, which can be the cation (+) or the anion (−). In CH_3CN, at 25 °C: $\lambda_o(Li^+) = 69.3$, $\lambda_o(Na^+) = 76.9$, and, $\lambda_o(ClO_4^-) = 103.7$, all in $cm^2\ \Omega^{-1}\ mol^{-1}$.[26]

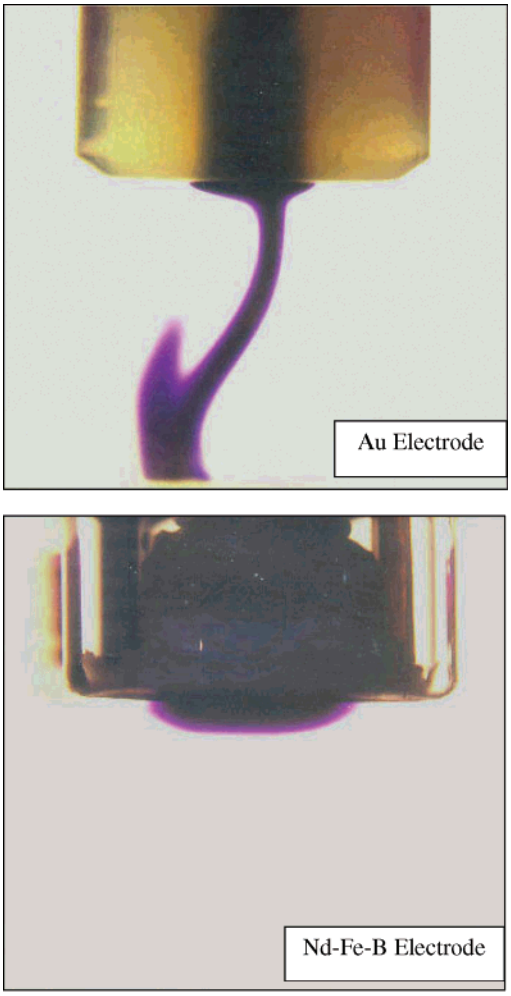

Figure 7. (Top) Photograph 10 s after a potential step (at 0.350 V vs Ag/AgCl) with a Au disk electrode (2 mm diameter) in an ~80 mM solution of TMPD in CH_3CN/0.5 M $NaClO_4$. (Bottom) Photograph 30 s after a similar potential step with a Nd−Fe−B magnet electrode (3.2 mm diameter) in the same solution. (The blue layer in front of the electrode is ~3.2 mm wide and ~0.6 mm thick.)

concentration of TMPD and a longer electrolysis time. In cyclic voltammetry, the latter is achieved with slower sweep rates. Generally, natural convection limits the lowest practical cyclic voltammetric sweep rates to ~0.02 V s^{-1}.[10b] Indeed, the inset of Figure 6A shows that, above ca. 0.02 V s^{-1}, the anodic peak current varies linearly with the square root of the sweep rate, in agreement with the Randles−Sevcik equation for a diffusion-controlled process.[10c] (Nevertheless, it should be noted also that even at 0.05 V s^{-1}, the shape of the cyclic voltammetric return wave is somewhat distorted, because of the longer electrolysis time and the inevitable onset of natural convection.)

Since the gravitational force density, $\mathbf{F}_g$, causing the phenomena of Figures 6A and 7 (top) is applied in the z-direction (Scheme 1), only the z-component of $\mathbf{F}_g$, $(F_g)_z$, is nonzero. The average value of $(F_g)_z$ per unit volume of the diffusion layer, $\langle (F_g)_z \rangle_{DL}$, is calculated via Newton's second law (eq 7) and the average density gain of the diffusion layer. The latter is

$$\langle (F_g)_z \rangle_{DL} = \langle C_{TMPD^{\bullet+}} \rangle_{DL} [t_{ClO_4^-} FW_{ClO_4^-} - t_{Li^+} FW_{Li^+}] |\mathbf{g}| \quad (7)$$

estimated from the average concentration of the positively charged $TMPD^{\bullet+}$ "injected" in the diffusion layer, $\langle C_{TMPD^{\bullet+}} \rangle_{DL}$,

and the fact that ($t_{ClO_4^-} \times 100$)% of that charge is compensated by ClO_4^- moving in and ($t_{Li^+} \times 100$)% by Li^+ moving out, as explained in the previous paragraph. $\langle C_{TMPD^{\bullet+}} \rangle_{DL}$ is considered equal to 40 mM, namely one-half of the sum of $C_{TMPD^{\bullet+}}$ at the two ends of the diffusion layer, FW_j represents the formula weight of species j, and $|\mathbf{g}|$ is the acceleration of gravity (9.81 m s^{-2}). It is thus calculated from eq 7 that $\langle (F_g)_z \rangle_{DL} = 22.3$ N m^{-3}.

Figure 6B shows the cyclic voltammogram of the same TMPD solution as above, using a Au-coated Nd−Fe−B magnet electrode (3.2 mm diameter), whose potential was swept again at 0.01 V s^{-1}. The solid-line voltammogram was obtained with the magnet electrode used alone, while the dashed-line voltammogram was obtained with the magnet electrode facing a second disk magnet (4.8 mm diameter) in the attracting configuration (refer to Scheme 1). The two voltammograms are essentially identical. Furthermore, it is clear both from the shapes and from the linear Randles−Sevcik plots (see inset) that these voltammograms are diffusion-controlled and uncomplicated by convection phenomena even at 0.005 V s^{-1}. This is confirmed again by looking at the electrode. The lower part of Figure 7 shows that, 30 s after a potential step in the mass-transfer-controlled range of TMPD with the 3.2 mm Nd−Fe−B magnet electrode, the diffusion layer (3.2 mm wide, 0.6 mm thick) is still in contact with the electrode. At much longer times (e.g.,100 s) the diffusion layer does not expand sidewise, but instead it appears bottom-heavy and eventually drops in analogy to Figure 7 (top). So, basically, the effect of the magnet electrode is to delay the onset of natural convection. It must be pointed out here that this response is quite general for diamagnetic species, and that analogous behavior has been obtained under similar conditions with nitrobenzene and *p*-benzoquinone. The absence of a magnetohydrodynamic stirring effect from Figures 6B and 7 (bottom) is not difficult to reconcile: first, under semi-infinite mass-transfer conditions the mass flux, and therefore the current density **i**, are both normal to any millielectrode; so, it is concluded that, under these experimental conditions, the angle between **B** and **i** is small (for this, consult also Figure 1A,B). Thereby, $\mathbf{F}_B$ (eq 1) is also very small, and magnetohydrodynamic convective effects are not observed. On the other hand, the absence of natural convection implies that the magnet electrode exerts an attractive force, at least equal and opposite to $\mathbf{F}_g$, that keeps the diffusion layer in contact with the electrode throughout the duration of the experiment. Let us discuss how.

Electrogenerated $TMPD^{\bullet+}$ is paramagnetic (a free radical with spin equal to $^1/_2$) and therefore renders the entire diffusion layer paramagnetic and susceptible to the two paramagnetic body forces, $\mathbf{F}_{\nabla B}$ and $\mathbf{F}_{\nabla C}$. Indeed, because the magnetic field in the vicinity of the magnet electrode is inhomogeneous ($\nabla \mathbf{B} \neq 0$), the diffusion layer may experience $\mathbf{F}_{\nabla B}$. Furthermore, because the concentration of $TMPD^{\bullet+}$ varies from a higher value close to the electrode to zero as the diffusion layer fades into the bulk solution, the diffusion layer will also experience $\mathbf{F}_{\nabla C}$. At this point it is self-evident that the z-components of $\mathbf{F}_{\nabla B}$ and $\mathbf{F}_{\nabla C}$, $(F_{\nabla B})_z$ and $(F_{\nabla C})_z$, respectively, are responsible for keeping the diffusion layer from falling, while the r-components, $(F_{\nabla B})_r$ and $(F_{\nabla C})_r$, respectively, are cylindrically symmetric and should determine only its shape. Since for linear diffusion $\partial C_{TMPD^{\bullet+}}/\partial r = 0$, $(F_{\nabla C})_r$ [$\sim(\partial C_{TMPD^{\bullet+}}/\partial r)$] $\neq 0$ only close to the outer limits of the diffusion layer and is directed inward. The role of $(F_{\nabla C})_r$ is to preserve the shape of the diffusion layer, irrespective of its size. On the other hand, $(F_{\nabla B})_r$ should be parallel to $(B\cdot\nabla B)_r$ (eq 2), and closer to the center of the magnet electrode, according to section 3, it should be directed outward, causing the expansion of the diffusion layer, but as the diffusion layer expands into areas where $(B\cdot\nabla B)_r$ is compressive (see Figures 3A and 5, and Appendix I in the Supporting Information), it experiences counterbalancing $(F_{\nabla B})_r$ forces directed inward. Overall, the diffusion layer does not expand beyond the radius of the electrode. In fact, the similarity between the shape of the diffusion layer in front of the magnet electrode in Figure 7 (bottom) and the borderline between the areas where $(B\cdot\nabla B)_r$ changes direction (Figures 3A and 5, and Appendix I) is immediately noticeable.

Now, let us discuss in detail why the diffusion layer will not fall. According to Figures 3 and 4, the $(B\cdot\nabla B)_z$ component of the $\mathbf{B}\cdot\nabla\mathbf{B}$ vector is directed toward the magnet electrode. Since $(F_{\nabla B})_z \sim (B\cdot\nabla B)_z$ (refer to eq 2), $(F_{\nabla B})_z$ holds the diffusion layer in contact with the electrode. Similarly, $(F_{\nabla C})_z \sim (\partial C_{TMPD^{\bullet+}}/\partial z)$ (refer to eq 3), and since $C_{TMPD^{\bullet+}}$ is higher at the electrode, $(F_{\nabla C})_z$ is directed toward the electrode, too. Of course, the question now is, which one of those two paramagnetic forces is stronger? To address that question, we conducted a relative magnitude analysis of $(F_{\nabla B})_z$ and $(F_{\nabla C})_z$ across the diffusion layer, by approximating the z-components of eqs 2 and 3 with difference forms (eqs 8 and 9, respectively)

$$\langle (F_{\nabla B})_z \rangle_{DL}|_r = 2N_A[(g\mu_B)^2/4kT]\langle C_{TMPD^{\bullet+}} \rangle_{DL} \langle (B\cdot\nabla B)_z \rangle_{DL}|_r \quad (8)$$

$$\langle (F_{\nabla C})_z \rangle_{DL}|_r = N_A[(g\mu_B)^2/4kT][\langle |\mathbf{B}|_z \rangle_{DL}|_r]^2[(\Delta C_{TMPD^{\bullet+}})_{DL}/\delta] \quad (9)$$

and introducing either calculated values or reasonable estimates of the various parameters. $\langle (F_{\nabla B})_z \rangle_{DL}|_r$ and $\langle (F_{\nabla C})_z \rangle_{DL}|_r$ are the average forces per unit volume in the z-direction across the diffusion layer at a certain distance r from the center of the magnet electrode. The spectroscopic splitting factor, g, was given the value of the free electron (2.00).[27a] $\langle C_{TMPD^{\bullet+}} \rangle_{DL}$ was defined above in conjunction with eq 7, and δ is the diffusion layer thickness. An upper limit for δ is estimated from the random walk equation $\delta^2 = 2D_{TMPD}\tau$, where D_{TMPD} ($=2.58 \times 10^{-5}$ cm^2 s^{-1}) is the diffusion coefficient of TMPD.[28] At the slowest sweep rate of Figure 6B (0.005 V s^{-1}), it takes $\tau = 70$ s for the potential to proceed from the onset of the anodic current ($\sim$0.0 V vs Ag/AgCl) to the point of the potential reversal (0.35 V vs Ag/AgCl). Thus, $\delta = 0.6$ mm. Meanwhile, the values of $|\mathbf{B}|$, B_z, B_r, $(B\cdot\nabla B)_z$, and $(B\cdot\nabla B)_r$ everywhere on the simulation grid have been tabulated and are provided in the Supporting Information. Using these tables, $\langle (B\cdot\nabla B)_z \rangle_{DL}|_r$, the average value of the z-component of the $\mathbf{B}\cdot\nabla\mathbf{B}$ vector across the diffusion layer at a certain distance r from the center of the magnet electrode, and $\langle |\mathbf{B}|_z \rangle_{DL}|_r$, the average value of the modulus of the **B** vector across the diffusion layer at a distance r from the center, were

(26) (a) Springer, C. H.; Coetzee, J. F. *J. Phys. Chem.* **1969**, *73*, 471. (b) Kay, R. L.; Hales, B. J.; Cunningham, G. P. *J. Phys. Chem.* **1967**, *71*, 3925. (c) Gill, D. S.; Tewari, J.; Singh, G.; Bakshi, M. S. *J. Chem. Soc., Faraday Trans.* **1991**, *87*, 1155.
(27) Drago, R. S. *Physical Methods in Chemistry*; W. B. Saunders Co.: Philadelphia, PA, 1977; (a) p 316, (b) p 425.
(28) Leventis, N.; Gao, X. *J. Electroanal. Chem.* **2001**, *500*, 78.

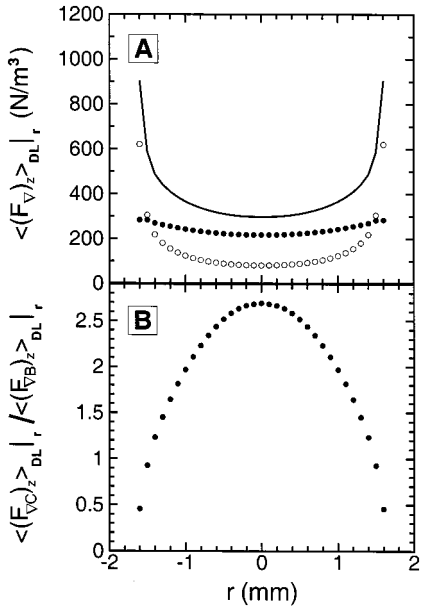

Figure 8. Nd−Fe−B magnet electrode alone. (A) Distribution along one electrode diameter ($-r_o \le r \le r_o$) of the average paramagnetic forces applied across the diffusion layer in the *z*-direction. Continuous line, $\langle(F_\nabla)_z\rangle_{DL}|_r$; open circles, $\langle(F_{\nabla B})_z\rangle_{DL}|_r$; dark circles, $\langle(F_{\nabla C})_z\rangle_{DL}|_r$. (B) Comparison of $\langle(F_{\nabla C})_z\rangle_{DL}|_r$ and $\langle(F_{\nabla B})_z\rangle_{DL}|_r$ across the diffusion layer over one electrode diameter.

calculated at the particular *r* via numerical integration of eq 10, where $f(z)$ stands for $(B\cdot\nabla B)_z$ or $|\mathbf{B}|_z$, respectively. Based

$$\langle f(z)\rangle_{DL}|_r = [\int_{z=0}^{z=\delta} f(z)\, dz/\delta]|_r \qquad (10)$$

on parameters calculated or estimated as just described, the values of $\langle(F_{\nabla B})_z\rangle_{DL}|_r$ and $\langle(F_{\nabla C})_z\rangle_{DL}|_r$ were calculated along the diameter of the magnet electrode (i.e., in the range $-r_o \le r \le r_o$), and the results are presented in Figure 8. From Figure 8 it is immediately apparent that (a) both paramagnetic forces are stronger than $\langle(F_g)_z\rangle_{DL}$ (=22.3 N m^{-3}) at all *r*, and therefore they could have retained the diffusion layer in contact with the electrode independently of one another, and (b) $\langle(F_{\nabla C})_z\rangle_{DL}|_r$ is generally a stronger force than $\langle(F_{\nabla B})_z\rangle_{DL}|_r$, except close to the perimeter of the magnet electrode, where the latter predominates (due to the rapid increase of the $B_r\,\partial B_z/\partial r$ term of $(B\cdot\nabla B)_z$; refer to Figure 4). Integration of $\langle(F_{\nabla B})_z\rangle_{DL}|_r$ and $\langle(F_{\nabla C})_z\rangle_{DL}|_r$ across the diameter of the magnet electrode yields $\langle(F_{\nabla C})_z\rangle_{DL} = 1.75\,\langle(F_{\nabla B})_z\rangle_{DL}$. It is noteworthy that despite the rapid increase of $\langle(F_{\nabla B})_z\rangle_{DL}|_r$ at the edge of the magnet electrode, $\langle(F_{\nabla B})_z\rangle_{DL}$ is not as strong as $\langle(F_{\nabla C})_z\rangle_{DL}$, and therefore the results of Figure 6B and the lower part of Figure 7 are mostly due to the latter.

By the same token, however, it should be pointed out that $\mathbf{F}_{\nabla C}$ is not always the overall dominant paramagnetic body force. As we shall see in this paragraph, there are situations in which $\mathbf{F}_{\nabla B}$ predominates, even with magnet electrodes of the size employed here. In that regard, Figure 9A shows that with our Au disk millielectrode, paramagnetic $[Co(bipy)_3]^{2+}$,[27b] being oxidized to diamagnetic $[Co(bipy)_3]^{3+}$, demonstrates a behavior analogous to that of TMPD (compare Figure 9A with Figure 6A); in contrast, with our Au-coated Nd−Fe−B electrode we observe no diffusion waves and quasi steady-state voltammograms essentially *independent* of the potential sweep rate (Figure 9B). This clearly points to a convection mechanism that behaves quite differently from natural convection. Specifically, the near

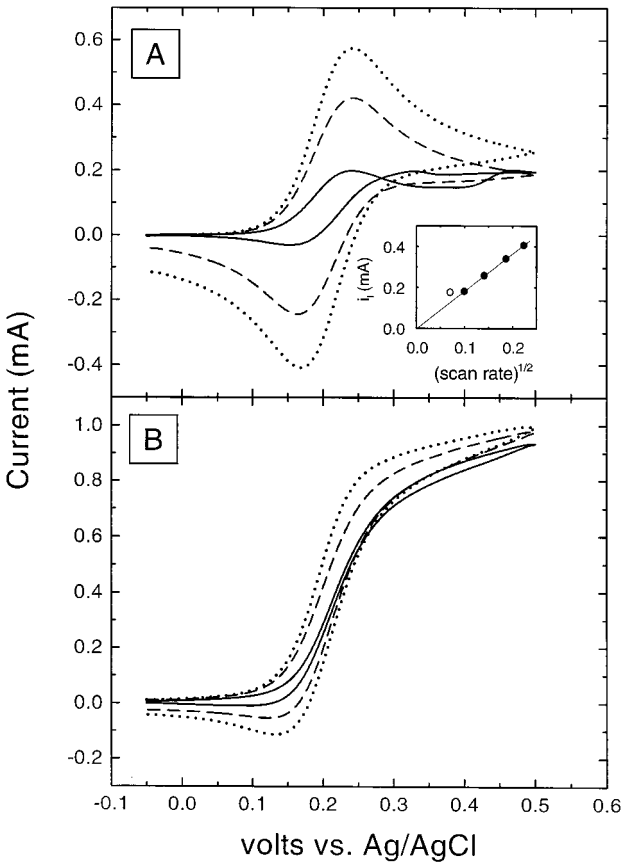

Figure 9. Cyclic voltammetry in an 80.1 mM solution of $[Co(bipy)_3](ClO_4)_2$ in CH_3CN/0.5 M $LiClO_4$. (A) Using a Au disk electrode (2 mm diameter). —, 0.01 V s^{-1}; − − −, 0.05 V s^{-1}; •••, 0.1 V s^{-1}. Inset: Randles−Sevcik plot. Dark symbols, peak currents; open symbol, plateau current (no identifiable peak). (B) Using a Nd−Fe−B disk magnet electrode (3.2 mm diameter). —, 0.01 V s^{-1}; − − −, 0.05 V s^{-1}; •••, 0.1 V s^{-1}.

insensitivity of the voltammograms to the potential sweep rate indicates that the main convection force does not depend either on the concentration gradient, which increases with the sweep rate, or on the amount of the material that is electrolyzed. Therefore, of the two paramagnetic body forces, $\mathbf{F}_{\nabla C}$, which depends on concentration gradients, should not be the dominant one. On the other hand, since the entire solution now contains paramagnetic $[Co(bipy)_3]^{2+}$, $\mathbf{F}_{\nabla B}$ is extended beyond the diffusion layer, is applied everywhere **B** and $\nabla\mathbf{B}$ have nonzero values, and is directed always toward the magnet electrode. Before electrolysis, $\mathbf{F}_{\nabla C}$ is zero everywhere, but $\mathbf{F}_{\nabla B}$, being already present, is stronger closer to the electrode, fading away in the bulk. Since $\mathbf{F}_{\nabla B}$ is weaker in the bulk, there is no tendency for solution farther from the electrode to replace solution closer to it. Therefore, the entire system is stable, and there is no convection. Once electrolysis is initiated, the neighborhood of the electrode is depleted of paramagnetic $[Co(bipy)_3]^{2+}$, and the balance of forces is destroyed. Since the concentration of $[Co(bipy)_3]^{2+}$ increases toward the bulk, $\mathbf{F}_{\nabla C}$ is directed away from the electrode, and therefore it tries to *remove* the diffusion layer. Meanwhile, an overall much stronger (because it is integrated over the entire solution) $\mathbf{F}_{\nabla B}$ force, acting mainly from the perimeter of the electrode, pulls paramagnetic solution from the bulk closer to the electrode to replace the mostly diamagnetic depletion layer. The paramagnetic forces now generate a funnel-like flow pattern, with solution taken up from the perimeter of the electrode and forced out from its center.

Before closing this section, we must address the possible impact of magnetophoretic phenomena in the interpretation of our results. As can be deduced from the diffusion-controlled behavior of Figure 6B, magnetophoretic mass transfer should not compete with diffusion within the time scale of that experiment. By and large then, when convection predominates over diffusion (as in Figure 9B), the possible role of magnetophoretic mass transfer should be even smaller. From a theoretical standpoint, we have reported recently that the flux $\mathbf{J}_j$ of a radical j in the absence of migration and convection is given by eq 11.[2] Assuming as before that at the mass-transfer-

$$\mathbf{J}_j = -D_j\nabla C_j + 2C_jD_j(g\mu_B/2kT)^2\mathbf{B}\cdot\nabla\mathbf{B} \qquad (11)$$

controlled limit $C_{TMPD^{\bullet+}}|_{z=0} \approx C_{TMPD,bulk} = 80$ mM, and $\delta = 0.6$ mm, it can be calculated that $(\partial C_{TMPD^{\bullet+}}/\partial z)|_{DL} \approx (\Delta C_{TMPD^{\bullet+}})_{DL}/\delta = 1.33$ mol m^{-4}, and therefore we can estimate the relative contributions of diffusion and magnetophoresis to the mass flux of $TMPD^{\bullet+}$ across the electrode. Thus, at the center of a magnet electrode, where $\langle(B\cdot\nabla B)_z\rangle_{DL}|_{r=0} = 80.1$ T^2/m, the diffusional flux is $\sim 2.0 \times 10^6$ times higher than the magnetophoretic flux, while at the edge of the magnet electrode, where $\langle(B\cdot\nabla B)_z\rangle_{DL}|_{r=r_o} = 617$ T^2/m, the diffusional flux is still $\sim 2.7 \times 10^5$ times higher than the magnetophoretic flux. Indeed, recently published magnetophoretic data under comparable field gradients (400 T^2/m) of paramagnetic water droplets in ethylbenzoate,[29] or of paramagnetic ions in silica gel,[30] support the view that paramagnetic volume transfer is a much faster process than magnetophoretic transfer of ions.

4.2. Voltammetry with a Magnet Electrode Facing a Second Magnet in the Repelling Configuration. With a second magnet held opposite to the magnet electrode in the repelling configuration of Scheme 1, the magnet electrode demonstrates quasi steady-state voltammograms with TMPD at 0.01 V s^{-1} (Figure 10A, solid line). However, this quasi steady-state behavior is lost quickly, and the magnet electrode shows strong diffusional characteristics even as early as 0.035 V s^{-1} (Figure 10A, dashed line). A direct view of the electrode after a potential step in the mass-transfer-controlled region (0.350 V vs Ag/AgCl) reveals a disk-shaped "diffusion" zone (Figure 10B) that is formed immediately after the potential step and extends sideways well beyond the diameter of the magnet electrode. (The blue layer is 4.6 mm wide and 0.6 mm thick.) After a short while (ca. 10 s), the part of the blue $TMPD^{\bullet+}$ envelope close to the electrode seems able to reach the outer edge of the magnet electrode assembly, and the blue radical flows *upward*. This situation appears stable for at least 100 s.

A qualitative understanding of the shape and size of the blue $TMPD^{\bullet+}$ envelope should come from consideration of the vertical and lateral forces. First, the blue layer is magnetized in the same direction as the magnet electrode, and therefore, it is repelled by the opposite magnet and is aligned parallel to the lines of force (Figure 1C). Now, in agreement with the general direction of the $\mathbf{B}\cdot\nabla\mathbf{B}$ vector shown in Figure 3B, $\mathbf{F}_{\nabla B}$ pushes the blue zone upward, toward the electrode. At the same time, $\mathbf{B}\cdot\nabla\mathbf{B}$ is expansive over the electrode at all z (i.e., its $(B\cdot\nabla B)_r$ component points outward) and compressive again at longer radial distances from the center of the magnet (refer to Figure 5, and the maps of $(B\cdot\nabla B)_r$ in Appendix I). Consequently, the blue layer is expected to expand sideways at longer distances (compared with the magnet electrode used alone) before the blue radical starts filling space where the lateral forces become compressive and counterbalance the expansive ones. Meanwhile, as in the case of the magnet electrode alone, the blue zone is prevented from falling by $(F_{\nabla B})_z$ and $(F_{\nabla C})_z$, which both point upward. Figure 11 presents the results of a relative magnitude analysis (through eqs 8−10) similar to that described in section 4.1. It is noted that close to the center of the electrode $\langle(F_{\nabla C})_z\rangle_{DL}|_r$ is almost 5 times stronger than $\langle(F_{\nabla B})_z\rangle_{DL}|_r$, and by integrating throughout the entire blue layer it is calculated that $\langle(F_{\nabla C})_z\rangle_{DL} = 1.77\langle(F_{\nabla B})_z\rangle_{DL}$. $\langle(F_{\nabla B})_z\rangle_{DL}|_r$ becomes stronger again near the "vertical" edges of the blue layer. Nevertheless, it should be pointed out that close to the center of the electrode $\langle(F_{\nabla B})_z\rangle_{DL}|_r$ is almost equal to $\langle(F_g)_z\rangle_{DL}$ (e.g., at $r = 0$, the former is equal to 26.4 N m^{-3}, and the latter to 22.3 N m^{-3}), and therefore it is doubtful whether it would be possible for $\langle(F_{\nabla B})_z\rangle_{DL}|_r$ to hold the diffusion layer alone, without $\langle(F_{\nabla C})_z\rangle_{DL}|_r$.

Now, the quasi steady-state voltammograms at conditions where, in analogy to Figure 6A, we would have expected diffusional behavior most probably indicate the presence of a convection mechanism other than natural convection; after all, natural convection of the type shown in Figure 7 (top) is not

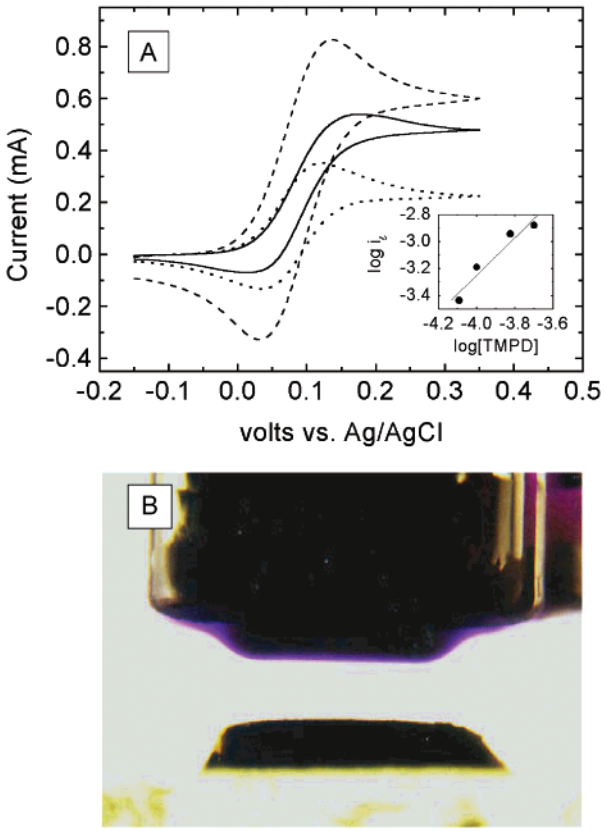

Figure 10. Nd−Fe−B magnet electrode (3.2 mm diameter) facing a second magnet (4.8 mm diameter) in the repelling configuration. (A) Cyclic voltammetry in an 81 mM solution of TMPD in CH_3CN/0.5 M $LiClO_4$. —, 0.005 V s^{-1}; − − −, 0.035 V s^{-1}. For comparison, ···, the magnet electrode with no opposing magnet, at 0.005 V s^{-1}. Inset: Double logarithmic plot of the limiting current at 0.005 V s^{-1} versus concentration. Slope = 1.3, correlation = 0.953. (B) Photograph of the two-magnet system 30 s after a potential step (at 0.350 V vs Ag/AgCl) in an ~80 mM solution of TMPD in CH_3CN/0.5 M $NaClO_4$. (The blue layer in front of the electrode is ~4.6 mm wide and ~0.6 mm thick.)

(29) Suwa, M.; Watarai, H. *Anal. Chem.* **2001**, *73*, 5214.
(30) Fujiwara, M.; Kodoi, D.; Duan, W.; Tanimoto, Y. *J. Phys. Chem. B* **2001**, *105*, 3343.

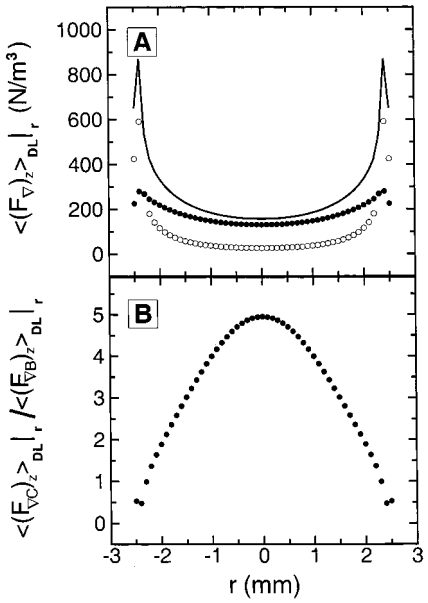

Figure 11. Nd−Fe−B magnet electrode facing a repelling magnet as in Figures 1C and 10B. (A) Distribution along the diameter of the blue layer of Figure 10B (-2.3 mm $\leq r \leq 2.3$ mm) of the average paramagnetic forces applied in the *z*-direction across the thickness of that layer (0.6 mm). Continuous line, $\langle(F_{\nabla})_z\rangle_{DL}|_r$; open circles, $\langle(F_{\nabla B})_z\rangle_{DL}|_r$; dark circles, $\langle(F_{\nabla C})_z\rangle_{DL}|_r$. (B) Comparison of $\langle(F_{\nabla C})_z\rangle_{DL}|_r$ and $\langle(F_{\nabla B})_z\rangle_{DL}|_r$ across the blue layer over its diameter.

observed. To investigate whether such a new convection mechanism actually exists, we have increased the concentration of TMPD and recorded the double logarithmic plot of the limiting current, i_l, versus $C_{TMPD,bulk}$. From our previous studies, it is known that strong magnetohydrodynamic convection, uncomplicated by other processes, yields linear log(i_l) versus log(C_{bulk}) plots with a slope equal to 1.34 and correlation coefficients ~1.0.[8a] Here, the log−log plot of the quasi limiting current i_l vs $C_{TMPD,bulk}$ is concave-down (see Figure 10A inset) with a superficial slope of 1.3. The curvature is attributed to natural convection, which starts to compete again as a mode of mass transfer as the concentration of TMPD increases.[31] These data support a magnetohydrodynamic effect that is due to the fact that the opposite magnet forces the **B** vector emerging from the magnet electrode into wide angles with the direction normal to the electrode, hence $\mathbf{F}_B (=\mathbf{i} \times \mathbf{B}) \neq 0$, and forces the solution to rotate as shown in Scheme 2. Using simulated values for B_r at $r = 0.5$, 1.0, and 1.6 mm from the center, and at $z = 0.6$ mm from the electrode surface (B_r = 0.077, 0.17, and 0.26 T, respectively; see Supporting Information), it is calculated that the values of $|\mathbf{F}_B|$ at the three *r*'s are 5.0, 10.6, and 16.2 N/m^3, respectively (i_l was taken from Figure 10A as equal to 0.5 mA, so $|\mathbf{i}| = 62.2$ A/m^2). Closer to the electrode surface, e.g., at $z =$ 0.2 mm, and at the same three radial distances as above, it is calculated that $|\mathbf{F}_B| = 5.0$, 11.9, and 27.0 N/m^3 respectively. By comparison, moderately strong magnetohydrodynamic stirring effects resulting from electrochemistry conducted in the field of 3 in. diameter Nd−Fe−B magnets are associated with

(31) The slope of the log(i_l) versus log($C_{TMPD,bulk}$) curve under natural convection conditions is 1.20, with a correlation coefficient equal to 1.0. (Leventis, N.; Gao, X., unpublished results.)

Scheme 2. A Second Magnet Held in Front of the Magnet Electrode in the Repelling Configuration (e.g., North-Facing-North) Bends the Magnetic Field Lines, So That $\mathbf{F}_B (=\mathbf{i} \times \mathbf{B}) \neq 0$ and Forces the Solution To Rotate

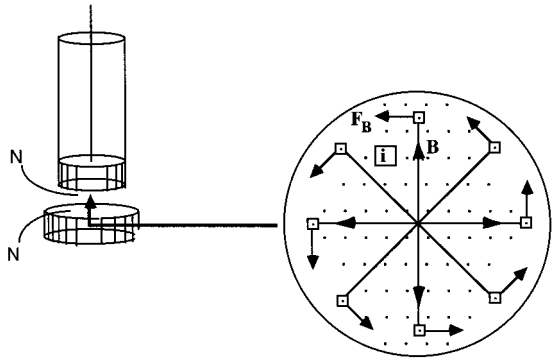

$\mathbf{F}_B$ forces in the order of 70 N/m^3.[2] The type of circulating flow proposed in Scheme 2 has been well established by White and co-workers around microelectrodes in homogeneous magnetic fields with **B** normal to their surface.[7] Here, however, the **i** vector is normal to the electrode, and **B** diverges out in analogy to the **i** vector at microelectrodes. The vortex of Scheme 2 is bound by the compressive paramagnetic forces in the radial direction. Nevertheless, the tangential $\mathbf{F}_B$ force, and therefore the resulting circulation, is more intense closer to the electrode. That partly explains the wider diameter of the blue TMPD$^{\bullet+}$ envelope closer to the electrode and the intriguing loss of material only from the circumference of the magnet electrode assembly. Meanwhile, mass balance must be maintained at all times, and that is most probably accomplished by an inward flux at the center of the vortex that increases the mass-transfer rate of TMPD, giving rise to the quasi steady-state voltammogram of Figure 10A.

5. Conclusions

During one-electron oxidation or reduction of diamagnetic species, electrodes made of Nd−Fe−B permanent magnets exert paramagnetic forces on the diffusion layer that delay the onset of natural convection. Of those forces, $\mathbf{F}_{\nabla C}$ is a stronger force than $\mathbf{F}_{\nabla B}$. With paramagnetic redox-active species, paramagnetic forces amplify the effects of natural convection. Holding a second magnet close to the magnet electrode in a repelling configuration generates modes of convection previously observed only with microelectrodes.

Acknowledgment. We gratefully acknowledge support from The Petroleum Research Fund (administered by the ACS, Grant No. 35154-AC5) and the University of Missouri Research Board.

Supporting Information Available: Appendix I, vector maps of $(B\cdot\nabla B)_r$ and $(B\cdot\nabla B)_z$ in the case of a magnet electrode alone and facing a second magnet in the repelling configuration; appendix II, tables with the values of B_r, B_z, $|\mathbf{B}|$, $(B\cdot\nabla B)_r$, and $(B\cdot\nabla B)_z$ in the space around the Nd−Fe−B magnet electrodes in the three configurations of Figure 1. This material is available free of charge via the Internet at http://pubs.acs.org.

JA0121991